Characterization and Mechanical Testing on Novel $(\gamma + \alpha_2)$ - $TiAl/Ti_3Al/Al_2O_3$ Cermet

HY. Li[a, *], P. Motamedi[a, b], J.D. Hogan[a]

[a] *Department of Mechanical Engineering, The University of Alberta, Edmonton, AB T6G 2R3, Canada*

[b] *Nanotechnology Research Centre, National Research Council Canada, 11421 Saskatchewan Dr., Edmonton, AB T6G 2R3, Canada*

Abstract

This study investigates the micro/nanostructural features and mechanical responses of a novel $TiAl/Ti_3Al/Al_2O_3$ cermet fabricated by self-propagation high-temperature synthesis. The microscopic diagnosis was used to examine the material composition, phase distribution, and elemental concentration of the cermet. Three phases were identified in the cermet, including γ-TiAl, α_2-TiAl, and Al_2O_3. The material exhibited ultrafine microstructure with the size of alumina particles between 0.5 microns to 1.5 microns occupying 65 ± 1% areal fraction of the material. Transmission electron microscopy (TEM) was employed to examine the "coral" network of alumina particles with the titanium aluminide matrix, which was believed to be contributing to the failure of the material. Iron/nickel-based nano-precipitates were found through TEM as well, and these were believed to be contributing to the mechanical properties of the material. The rate-dependency on the compressive strength and failure mechanisms were studied by quasi-static and dynamic uniaxial compression, and it was found that the quasi-static and dynamic compressive strengths were 2400 ± 120 MPa and 3370 ± 450 MPa, respectively. The results are compared with

* Corresponding author

Email addresses: haoyang@ualberta.ca (HY. Li), pouyan1@ualberta.ca (P. Motamedi) jdhogan@ualberta.ca (J.D. Hogan).

those for alumina AD995, to highlight differences in mechanical properties, such as compressive strength and failure strains. These findings serve as the preliminary dataset for material design, manufacturing, and modeling of advanced cermets.

Keywords: Cermets; microstructural characterization; uniaxial compression test; rate-dependency; compressive strength; failure mechanisms; material design and manufacturing

1. Introduction

Metal matrix composites (MMCs) are among the emerging materials for structural applications which have been extensively studied over the past century. Cemented carbide was the first major MMC invented in the 1920s. It was mainly used as cutting tools due to its superior hardness, when compared to conventional metals and ceramics. However, its high density (15.9 g/cm^3) limited its usage in applications, where high strength-to-weight ratio was required (e.g., body armor, turbine blades). In the 1930s, the term "cermet" was created to distinguish other ceramic-metallic composites, which consist mainly of carbides other than WC [1]. In 2001, Daniele Mari defined three classes of cermet by their refractory components [2]. The first class was called "hardmetal," and this consisted of ceramics that were constituted of carbides, nitrides, borides, and silicides of the metals in the fourth to six groups of the periodic table. The second class was termed "cermet," and this consists of some of the hardest carbides and nitrides like SiC and B_4C. Large differences in elastic modulus and thermal expansion from metals usually made these cermets of little practical interest. The third class was called "oxide cermet," which consists of oxide ceramics like Al_2O_3 and ZrO_2. This class of materials' high resistance to chemicals and the refractory character of these oxide ceramics has stimulated engineering research effort towards cermet development for dental [3] and high strain rate applications [4].

Interest in using cermets to replace advanced ceramics in body armor has existed since the 1970s (and likely before). This was motivated by the ability to add increased ductility to cermets, which was believed to augment their impact performance through a reduction in the depth of penetration and delayed axial cracking [4]. The seminal work of Wilkins et al. [4] in 1969 and Landingham and Casey [5] in 1972 also demonstrated the importance of microstructure (e.g., size and distribution of ceramic phase in the metal) on the impact performance of cermets. This work served as the foundation for the subsequent studies, which increased in frequency in the 1990s when fabrication technologies were able to produce cermets at near 100% theoretical densities with comparable hardness and densities to conventional advanced ceramics (e.g., alumina at ~4 g/cm^3). Examples include: Al_2O_3-Al (3.53 to 3.74 g/cm^3) [6], TiB_2-B_4C (3.25 g/cm^3 to 3.6 g/cm^3) [7], Cr-Cr_2S_3 (4 g/cm^3 to 5.4 g/cm^3) [8], and B_4C-Al cermet (2.62 g/cm^3) [9]. The further integration of these materials in protection applications requires a better understanding of their rate-dependent behavior, which is addressed in this paper.

Previous studies on cermets have shown that mechanical properties and fracture mechanisms are rate-dependent, and this is important for their use in ballistic protection applications. For example, Rittel et al. [10] found that the dynamic fracture toughness of TiC/1080 steel cermet is significantly higher (by about a factor of 3) than its quasi-static counterpart. In another study, Kaplan [11] and his colleagues showed that this increase was likely due to the change in fracture mechanisms from quasi-static to dynamic condition by visualizing the change in the crack path with the help of transmission electron microscopy. Rate-dependent effects for the compressive strength were also studied in WC-Co system by Mandel et al. [12], where it was found that the compressive strength increased with increasing strain rate, from 4370 MPa for WC-12Co under quasi-static loading to 6660 MPa for WC-6Co under dynamic loading (~ 1.5 times higher). Guden and Hall [13] also

reported a difference in compressive failure stress with increasing strain rate (10^{-5} to 7 x 10^{2} s^{-1}) for an Al/Al_2O_3 cermet. Other studies on the rate-dependency of cermets have been showing significant changes under dynamic loading in both property and mechanisms [14 – 16]. Understanding the complex rate-dependent response of cermets is essential to further improving their usage in dynamic applications (e.g., body armor). We study these aspects in this paper for a novel ($\gamma + \alpha_2$) - $TiAl/Ti_3Al/Al_2O_3$ cermet.

The ($\gamma + \alpha_2$) - $TiAl/Ti_3Al/Al_2O_3$ cermet belongs to the "oxide cermet" class. This cermet is relatively new in the open literature (e.g., Shen et al. [17]), with limited information on its mechanical responses. Xiang et al. [18], Zhang et al. [19], and Huy et al. [20] only reported the quasi-static hardness and fracture toughness values of the as-fabricated cermets, with no rate-dependent information available in their studies. Instead, most of the available literature has focused on sintering and forging techniques, such as the Self-Propagation High-Temperature Sintering process (SHS) [20 – 22]. In these studies, some mechanical properties, such as density and toughness, have been calculated by chemistry means (e.g., density of state method (DOS), band structure, and chemical bonding) [17]. To address the gap in knowledge on the mechanical response of this material, this paper explores the mechanical behavior of the $TiAl/Ti_3Al/Al_2O_3$ cermet under both quasi-static and dynamic loading. Prior to the experiments, surface microscopy was first used to examine the microstructure and composition of the as-received material. This included scanning electron microscopy (SEM), transmission electron microscopy (TEM), x-ray diffraction (XRD), and energy-dispersive x-ray spectroscopy (EDS). Secondly, mechanical testing was carried out on a standard MTS machine at quasi-static strain rates and split Hopkinson pressure bar (SHPB) for dynamic strain rates. Mechanical properties and material performance under different loading conditions were compared with alumina AD995, which is an advanced ceramic

that is being used in many defense applications. The results gathered in this study can facilitate the understanding of the microstructure-property relationship, which is crucial in the design of next-generation protection materials.

2. Material

The as-received material is manufactured by Lumiant Corporation, British Columbia. The $TiAl/Ti_3Al/Al_2O_3$ cermet, commercially known as TitanMade L465, is fabricated through Self-Propagation High-Temperature Sintering. The powders used for sintering are titanium dioxide and aluminum. The primary and secondary reactions were well documented in Shen et al. [17] and Gaus et al. [23]. Once synthesized, the material is received as plates, and these plates are cut into cuboidal specimens with sizes of 2.3 mm x 2.5 mm x 2.7 mm by electrical discharge machining (EDM) for mechanical testing. Table 1 summarizes the mechanical properties of the material provided by the company. Comparable data for alumina AD995 (by Coorstek. Inc.) [24] is also shown in Table 1, and this is drawn upon later in the discussion when comparing the two materials. Note that all properties reported are measured by standard techniques under quasi-static condition. Shown in Table 1, the cermet has comparable density with alumina AD995 with an increase in flexural strength and fracture toughness, but with lower stiffness and hardness. This can serve as a preliminary observation on the effect of combining ceramic and metallic materials (in this case, intermetallic to be more specific). To explore the hardness and stiffness properties of the individual titanium aluminide and alumina phases, nanoindentation testing was performed by Anton Paar [25] on the Ultra Nanoindentation for 900 indents on an area of 270 μm x 270 μm using a peak load of 1 mN. The elastic moduli for titanium aluminide and alumina phases were found to be 178 ± 31 GPa and 278 ± 41 GPa, respectively. The hardnesses for the two phases were 8 ± 2 GPa for the titanium aluminide phase and 22 ± 8 GPa for the alumina phase. Nanoindentation testing with the

same setup was performed on alumina AD995 as well, which gave a hardness of 23 ± 11 GPa. These values are also shown in Table 1 as nano-hardness.

Table 1: As-received mechanical properties with comparison to 99.5% purity Alumina by Coorstek. Inc.

	TitanMade L465	Al_2O_3 (AD995)
Density (g/cm^3)	3.9	3.9
Stiffness (GPa)	280	370
Hardness (GPa)	11	14.1
Flexural Strength (MPa)	925	375
Fracture Toughness (MPa $m^{1/2}$)	7.4	4 – 5
Nano-Hardness (GPa)	8 ± 2 (titanium aluminide) 22 ± 8 (alumina)	23 ± 11

3. Experimental Setup

3.1. Scanning electron microscopy and energy-dispersive x-ray spectroscopy

Scanning electron micrographs were taken of the polished surface (sub-micron) of the material by using a Zeiss Sigma FESEM machine equipped with an energy-dispersive x-ray spectroscopy setup. The machine is equipped with a field emission electron gun. No coating was needed for the specimen since conductivity was an inherent property of the intermetallic phase in the composite. The electron high tension (EHT)/accelerating voltage was set at 20.00 kV, and the working distance (WD) was at 8.5 mm. An In-Lens detector (ILD) coupled with a back-scattered detector (BSD) was used in this study to reveal the phase distribution within the material. EDX data was examined using the AZtec software from Oxford Instruments.

3.2. Transmission electron microscopy

Transmission electron microscopy was conducted using a JEOL JEM-ARM200CF S/TEM tool. The tool was operated at 200 kV, and the data was analyzed using the Gatan Digital Micrograph software. An energy-dispersive x-ray spectroscopy detector was coupled with TEM to examine

the nanoscale composition of the cermet. Specimens for this investigation were cut to a cross section of 2.5 mm x 2.5 mm using a diamond wafer blade and mechanically grounded from the bulk specimens down to ~ 50 μm in thickness with a 15 μm grid diamond paste. This was followed by mechanical dimpling to 30 μm, and ion milling (Ionfab 300 IBE) with a 4-inch diameter ion gun (8kV for 1 hr, 5kV for 45 mins, and 3kV for 40 mins) in an argon environment on a single wafer system to perforation.

3.3. X-ray diffraction

X-ray diffraction (XRD) analysis was carried out to assess the crystallinity and identify the phases. The tests were carried out on a Bruker D8-Discover machine using Cu Kα beam source. The apparatus was operated at 50 kV and 1000μA. A Vantec 500 detector was used to produce two-dimensional frames, which were then processed using the Bruker Eva software to produce θ-2θ-equivalent spectra.

3.4. Quasi-static uniaxial compression

The quasi-static uniaxial compression tests were carried out on a standard MTS series 810 servo-hydraulic machine. Shown in Figure 1 is the schematic of the quasi-static test setup. The loading platens were made from M2-graded high-speed steel (HSS) with diameter of 1 inch, and these were used to compress the specimen. Ti-6Al-4V titanium alloy jacketed tungsten carbide (WC) platens were used between the specimen and the loading platens to provide stress re-distribution from the specimen to the loading platens, as well as to reduce indentation from the harder material to the loading platens. This follows the ASTM C1424-15 standard [26]. As required, extreme pressure grease was applied on the WC platen surfaces as lubricant to eliminate the frictional effect. The platens were pre-loaded without specimen to create a thin, uniform layer of lubricant. The specimens were then carefully placed at the middle of the platens. Proper alignment was ensured

by carefully bringing the platens and specimen in touch. The experiment was performed under a displacement control setting with a nominal strain rate of 1 x 10^{-4} s^{-1}. The cross-head displacement was measured by a linear variable differential transformer (LVDT) displacement sensor with an accuracy of 0.001 mm. A 100 kN load cell with a background noise of approximately ± 1 N was used to record the force history during the loading process. The acquisition rate of the MTS machine was set at 30 Hz. Coupled with the testing setup was a high-speed AOS PROMON U750 camera to provide visualization of macroscopic deformation features on the specimen surface. The specimen was positioned normal to the optical axis of the camera to eliminate out-of-plane displacement. This camera has a full resolution of 1280 x 1024 pixels and recorded at a frame rate of 100 frames per second. The experiment was stopped when catastrophic failure happened. The engineering stress was calculated by dividing the applied load by original specimen surface area. In total, ten experiments were presented in this study at the same loading condition to ensure repeatability.

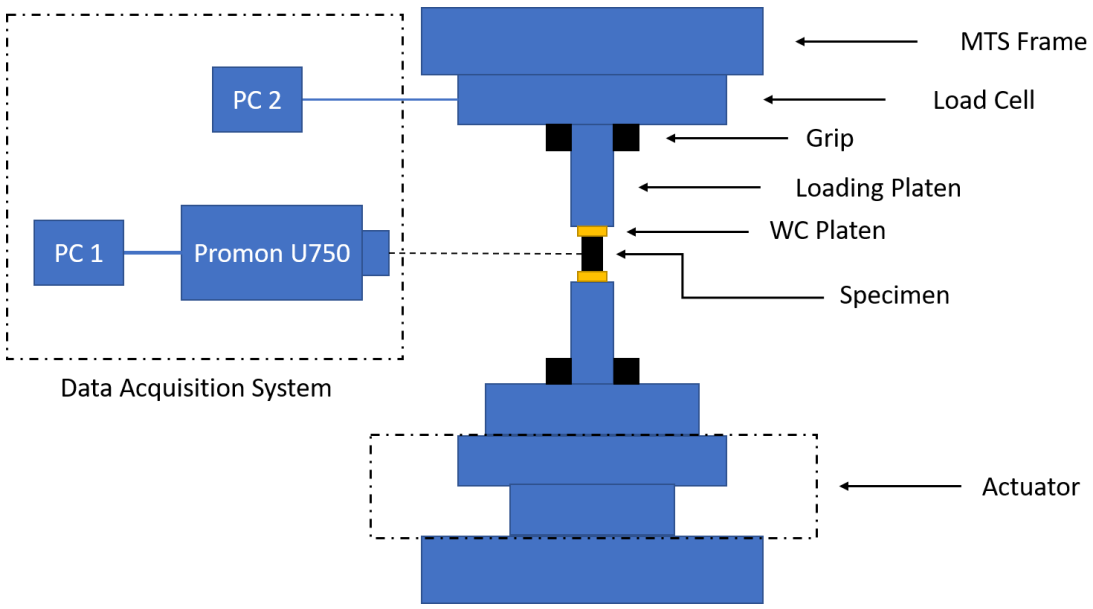

Figure 1: Schematic of the MTS machine experimental setup.

3.5. Dynamic uniaxial compression

The dynamic uniaxial compression tests were conducted on a modified version of a split Hopkinson pressure bar (SHPB). In a dynamic uniaxial compression test with conventional SHPB setup, the striker is launched from a pressurized gas gun and strikes the incident bar. An elastic stress wave is generated and travels through the incident bar towards the front end of the specimen. Due to the mismatch of impedance between the steel and the cermet, a reflected wave and a transmitted wave will be generated at the front and end faces of the specimen, respectively. The reflected wave travels back to the incident bar, and the transmitted wave travels through the transmitted bar. By capturing the pulse information with strain gauges, the stress, strain and strain rate can then be calculated.

In this paper, like some others for ceramics [27] [28], we plot the stress vs. time to understand the failure processes during loading. The nominal axial stress in the specimen is determined as,

$$\sigma(t) = E_0 \frac{A_0}{A_s} \varepsilon_t(t) \tag{1}$$

where A_s (m^2) is the cross-sectional area of the specimen, A_o (m^2) is the cross-sectional area of the bar, and ε_t is the time-resolved transmitted strain. Note that the equation above assumes that the specimen is deformed homogeneously and the bar deforms elastically during loading.

A modified version of the conventional setup needs to be adapted for testing brittle materials [29]. Shown in Figure 2 is the schematic of a modified version of the SHPB setup used in this study. The setup consisted of a gas gun, a striker, an incident bar, a transmitted bar, and an acquisition system. The acquisition system included amplifiers and a digital oscilloscope. The striker, incident bar, and transmitted bar were made from Maraging steel C-350. The stiffness of the material was 200 GPa with a yield strength of 2.36 GPa. The high stiffness and strength of the bars were required

for testing stiff materials, such as ceramics and cermets. Similar materials have been used for ceramics and cermets testing [14] [29]. The dimensions of the bars used in this study were 1016 mm and 914 mm in length for the incident and transmitted bar, respectively, with a common diameter of 12.7 mm. In this study, both the incident and reflected waves were captured by a strain gauge mounted on the incident bar, which has a distance of 662 mm to the front face of the specimen. The transmitted wave was captured by the strain gauge mounted on the transmitted bar, which has a distance of 310 mm to the end face of the specimen. The length of the bars and the position of strain gauges were chosen to avoid signal overlapping. Both strain gauges were 350Ω ± 0.3% with a gage factor of 2.130 ± 0.5% (made from Micro 184 Measurements CEA-13-250UN-350). Two independent conditional amplifiers (Vishay InterTechnology 2310B) were used for both gauges. The gains were set at 10 times on both amplifiers. A Tektronix DPO2024B oscilloscope was used to capture the signal. The resolution of the oscilloscope was 12-bit recording at 500 MHz. A short striker (125 mm) was used based on the observation on the pulse duration in the trial tests.

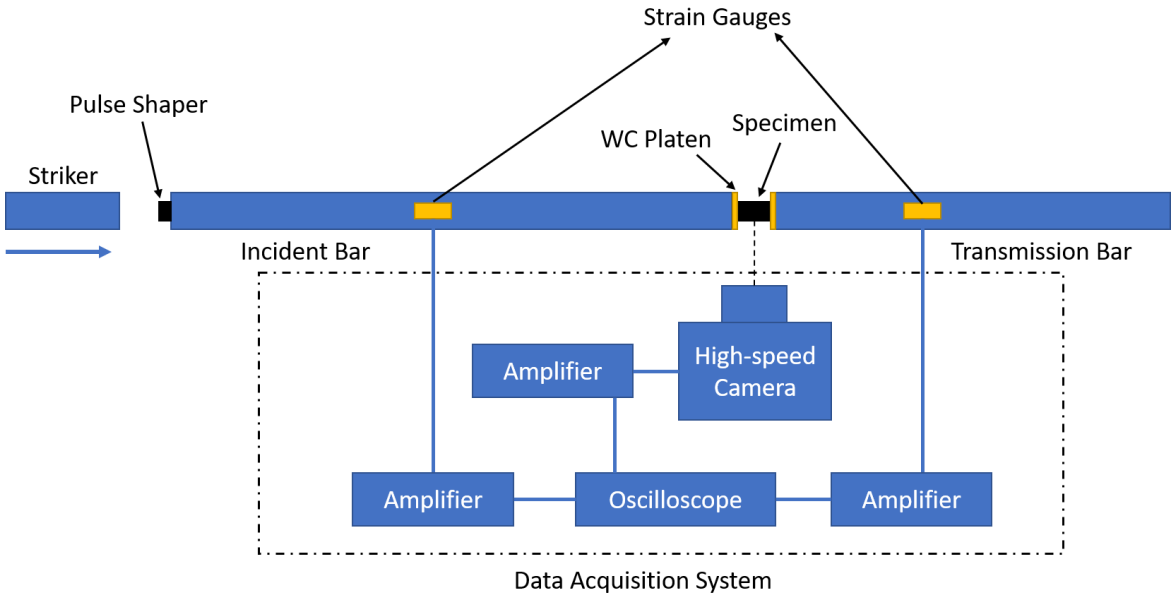

Figure 2: Schematic of the modified Split Hopkinson Pressure Bar (SHPB) experimental setup.

Two impedance matched Ti-6Al-4V titanium alloy jacketed tungsten carbide (WC) platens with the same diameter of the bars were attached to the end of the incident and transmitted bar for re-distribution of loads. This has been reported by Chen and Ravichandran [29] for preventing indentation and reducing stress concentration on the specimen. The specimen was placed between the two platens. The end faces of the specimen were lubricated with extreme pressure grease to reduce the frictional effect and allow the specimen to expand freely in the radial direction during loading. This setup is well documented in the literature [30] [31].

A pulse shaper was placed at the impact end of the incident bar to create a favorable profile of the pulse for the specific material. Trial tests were performed by assuming a brittle nature of the cermet based on the knowledge of the phases present. Pulse shapers with different materials and thickness were tested, and elastic tests were conducted with these pulse shapers beforehand to determine an appropriate rise time and ramp time, as well as ensuring force balance and constant strain. In these experiments, a mild steel pulse shaper was selected, and this is consistent with the literature [57 – 59]. The mild steel pulse shaper used in this study had a thickness of 0.0635 mm, and this was selected to give the most reasonable rise time and ramp time, for which the natural responses of the material could be well captured.

An ultra-high-speed Shimadzu HPV-X2 camera was used to capture the failure process of the specimen during SPHB testing. Exposure times of 200 ns were obtained using ultra-bright LED light attached with fiber optical light guide with an outer diameter of 7.6 mm so that the light can be concentrated onto the specimen surface. The camera was triggered by a split signal from the incident strain gauge. A separate conditional amplifier was coupled with the oscilloscope for camera triggering. In all experiments, the camera operated at 2 million frames per second with a resolution of 400 x 250 pixels. At this rate, the camera was able to capture 128 frames in total. The

output pulse of the camera was used to correlate the times between images and strain gauge measurements. Five tests were performed under the same loading conditions to verify the repeatability of experiments.

4. Experimental Results

4.1. Material Microstructure and phase distribution

Shown in Figure 3 is a BSE-SEM image (Fig. 3-a) with EDS concentration mapping on the elements: Al (Fig. 3-b), O (Fig. 3-c), Ti (Fig. 3-d). Overall, this figure is used to present a representative phase distribution within the material. In the BSE-SEM image, the lighter regions correspond to the TiAl phase because of the higher atomic number value. Consequently, the darker regions corresponded to the Al_2O_3 (alumina) phase. The darkest spots in Fig. 3-a correspond to the micropores present in the material, which tend to cluster around or within the alumina phase. This has been confirmed with FESEM images taken at the same location. It is observed that most of the alumina particles cluster to form a network with very few individual particles distributed sparsely over the matrix. A "coral" network of alumina phase is proposed to describe this microstructural feature, and this is believed to be the result of the rapid sintering process. Similar "coral" network has been observed in $TiAl/Ti_3Al/Al_2O_3$ cermet by Huy et al. [20] using Combustion Sintering. Next, image processing in MATLAB is used to examine the areal percentage of each phase and porosity level. To do this, the BSE-SEM image is first converted to a binary image. Each pixel is discretized and assigned a number from 0 to 255 as a Unit8 type image. In this case, pure white corresponds to 255, and pure black is 0. Thresholds based on gray level are then manually selected to isolate the titanium aluminide and alumina phases, as well as the pores. As the outcome of the analysis, the porosity level is found to be between 1.2 % and 3% at 2000 times magnification, with the uncertainty associated with the range of threshold values chosen. The area fraction of the

alumina phase is estimated at 65 ± 1%, using similar methodology. The 1% uncertainty is associated with a ± 20% grayscale threshold determined manually to compensate for any human errors. By using the same procedure, the pore size is found to be between 0.03 and 1 μm with an average of 0.15 ± 0.21 μm. This range of pores includes the structural and sub-structural pores in the material. The size of individual alumina particles is between 0.5 and 1.5 μm with an average of 1.0 ± 0.3 μm. The size of the alumina clusters is between 3 and 9 μm. All information above has been confirmed with other BSE-SEM images taken at different locations with different magnifications. Five specimens are also used to ensure the microstructural variability is taken into account.

Next, we consider the concentrations of the elements in Fig. 3-b to d. A color bar is presented as a reference to concentration for visualization. In the images, a brighter color indicates higher concentration while a darker color indicates a lower concentration. In Fig. 3-b, it is confirmed that Al is present everywhere in the material, but it is highly concentrated in the alumina phase (darker phase in BSE-SEM image in Fig. 3-a). Comparing Al (Fig. 3-b) with Ti (Fig. 3-c), it is observed that regions of high concentrations of Al correspond to regions with low or little concentration of Ti. The dark regions in Fig. 3-c confirm that there is little to no Ti in the alumina phase. Similarly, regions with higher concentration of Al overlap with regions with higher concentrations of O, which are the alumina phase. However, it is clear that some O exists in the TiAl phase regions, which indicates a high possibility that a secondary phase is present in the material. For this cermet, this phase is a α_2-Ti_3Al or (γ + α_2) lamellar structure since it is easier for oxygen to precipitate in these two phases during the sintering process [17] (confirmed next in XRD scanning).

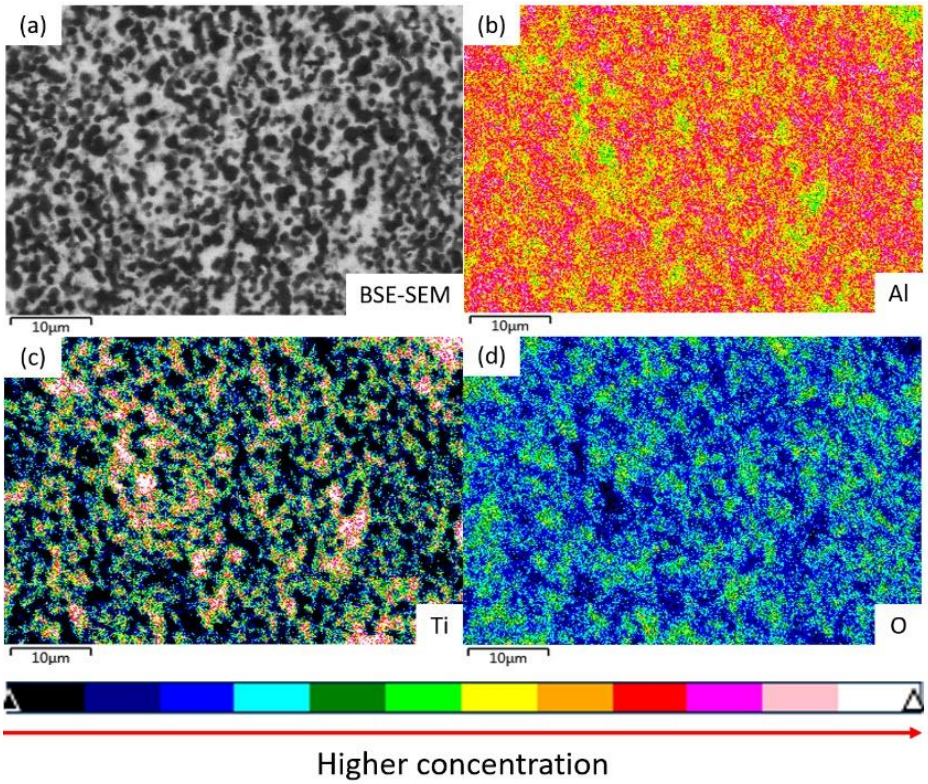

Figure 3: EDS concentration mapping with BSE-SEM image showing the distributions of selected elements. The concentration of the elements is ordered based on the color sequence in the visible light spectrum with a color bar shown below the maps. (a) FESEM image showing the phase distribution, where the black regions correspond to the alumina phase and the white regions correspond to the titanium aluminide phase; (b) Distribution and concentration of Al in the FESEM image; (c) Distribution and concentration of O in the FESEM image; (d) Distribution and concentration of Ti in the FESEM image.

To summarize the elemental analysis results, we show the weight and atomic percentage of the primary and secondary elements in Table 2. This is extracted from the EDS mapping presented above (see Fig. 3). Oxygen is the dominant element in both weight and atomic percentage, with 35.4% and 50.5%, respectively. This is followed by aluminum and titanium, which is expected since the alumina phase occupies 2/3 of the material in terms of volume. Carbon, zirconium, and potassium appeared in relatively low percentage in the material, with 4.5%, 0.9%, and 0.2% in weight percentage, respectively. It is believed that the trace of carbon is from the carbon adhesive

for attaching the specimen. The source of zirconium and potassium is likely impurities in the original mixing powders.

Table 2: The weight and the atomic percentage of the primary and secondary elements present in the EDS scan. Here carbon, zirconium, and potassium are considered as the secondary elements in the material.

Element	wt%	at%
O	35.4	50.5
Al	34.0	28.8
Ti	25.0	11.9
C	4.5	8.5
Zr	0.9	0.2
K	0.2	0.1

4.2. Material composition

Shown in Figure 4 is the diffraction spectrum from the x-ray diffraction analysis. The results presented here indicate that three phases are present in the specimen: 1. γ-TiAl, 2. alumina (Al_2O_3), and 3. α_2-Ti_3Al. The α_2-Ti_3Al phase is considered to be a by-product of the SHS process, during which the α_2-phase is introduced into the material through chemical reactions. This has been documented in the literature for this type of cermet [17] [20]. A minor trace of oxygen is detected in the α_2 phase, where the element exists in the EDX mapping of the TiAl phase (Fig. 3-d) as well. It has been reported that the (γ+α2) lamellar structure formed from the co-existence of individual γ- and α_2-phases could have a positive effect on the material toughness and ductility, given higher oxygen solubility and oxide precipitation at the interface [17], although this is not the focus of the current study.

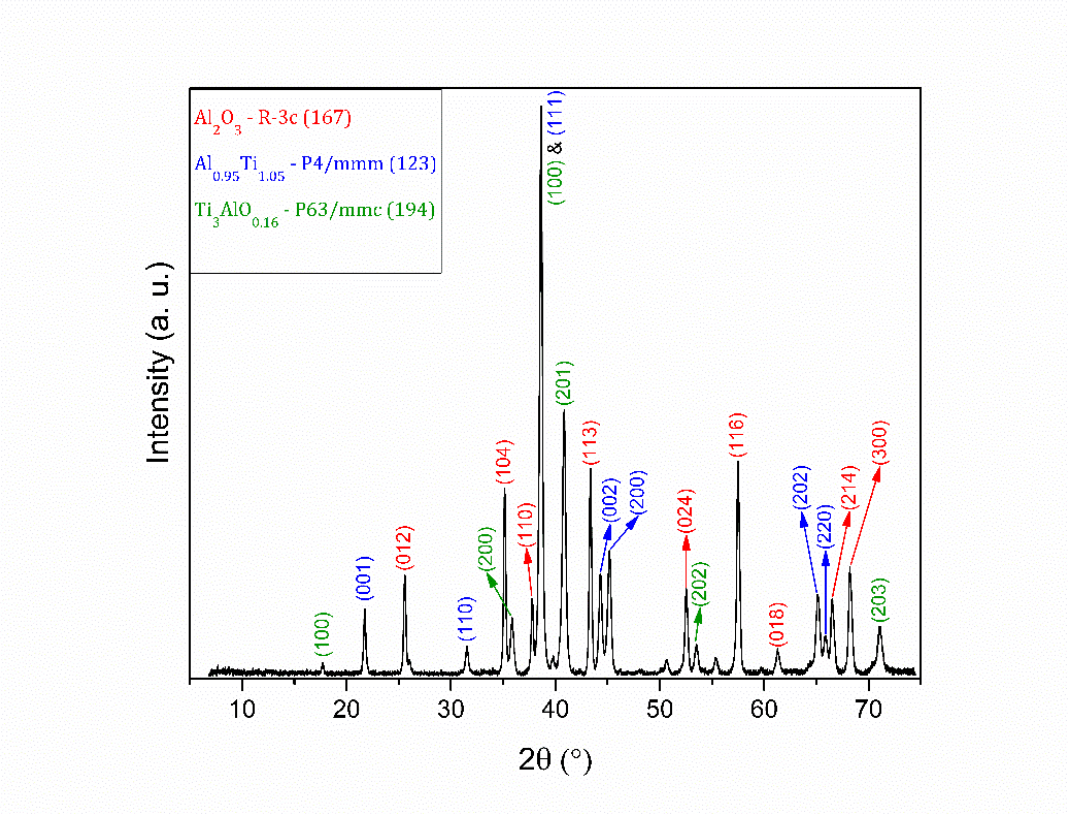

Figure 4: XRD spectrum of the cermet showing three distinct phases presented in the material. The legend shows the phases associated with each color, along with their corresponding space groups.

4.3. Nanoscale microstructural features

Shown in Figure 5 is a collection of transmission electron micrographs of the cermet. TEM was used to examine the detailed features of the phases and grains. At the sub-micron scale, individual alumina grains can be observed in Fig. 5-a (darker regions) and alumina particles packed with closely bounded interfaces are identified as the "coral" clusters in the material. This can be verified by the EDS mapping of Ti shown in Fig. 5-b. From the EDS map, the alumina particles are interconnected and non-uniformly distributed in the microstructure. Shown in Figure 5-c is the grain boundary of two titanium aluminide grains. Multiple locations are scanned, and minimal signs of plastic deformation, such as dislocations and twinning, is observed on these grains. Grain boundaries appear to be free of additives, and no microcracks are observed on the grains or along

the interface. Nano-precipitates (black dots) are observed throughout the material (including titanium aluminide and alumina phases) at higher magnification, and this feature is not resolvable by SEM or EDX on the bulk specimen.

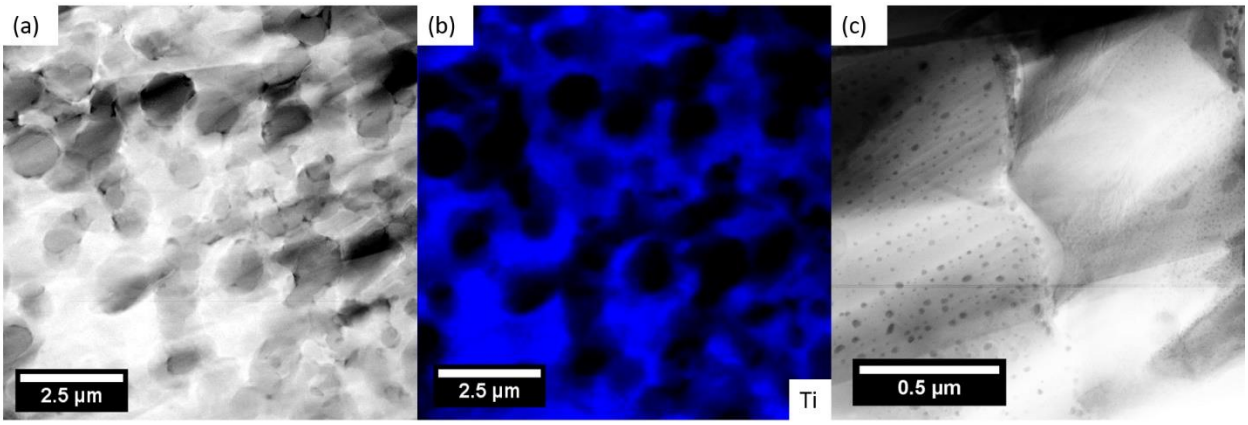

Figure 5: Transmission electron micrographs showing: (a) Individual alumina particles (darker) and the "coral" network formed by connected alumina particles under bright field mode, (b) corresponding EDS map of titanium further proves the composition of particles and highlights the alumina network, and (c) the grain boundary between two titanium aluminide grains.

Next, EDS is performed on the TEM images to determine the compositions and distributions of these nano-precipitates. Shown in Figure 6-a is the TEM micrograph taken of a single titanium aluminide grain. The nano-precipitates are dispersed over the entire grain, with sizes between 10 and 40 nm and an average of 17 ± 6 nm. To further investigate the composition of the nano-precipitates, EDS mapping was performed at the same location, and the results are shown in Figure 6-b and c. From the images, iron and nickel elements are present in these nano-precipitates. The bright dots in Figure 6-a correspond to high concentrations of iron and nickel in Figure 6-b and c. Multiple locations are examined to confirm the universality of this observation. As an outcome, these nano-precipitates disperse uniformly throughout the entire material, including in the alumina phase. It is suspected that these nano-precipitates are in the form of a metallic or oxide phase of the two elements under high temperature and high pressure sintering conditions. According to the

phase diagram of the Al-Ni-Ti system [32] and Al-Fe-Ti system [33], the nano-precipitates are likely to appear in a metallic form in the titanium aluminide phase. By consulting the phase diagram of the NiO-Al_2O_3 system [34] and Al_2O_3-Fe_2O_3-FeO system [35], the nano-precipitates are likely to appear as their oxide form in the alumina phase. It is believed that their existence stems from the impurities in the original aluminum powder used for sintering or from the equipment used to transport the powders.

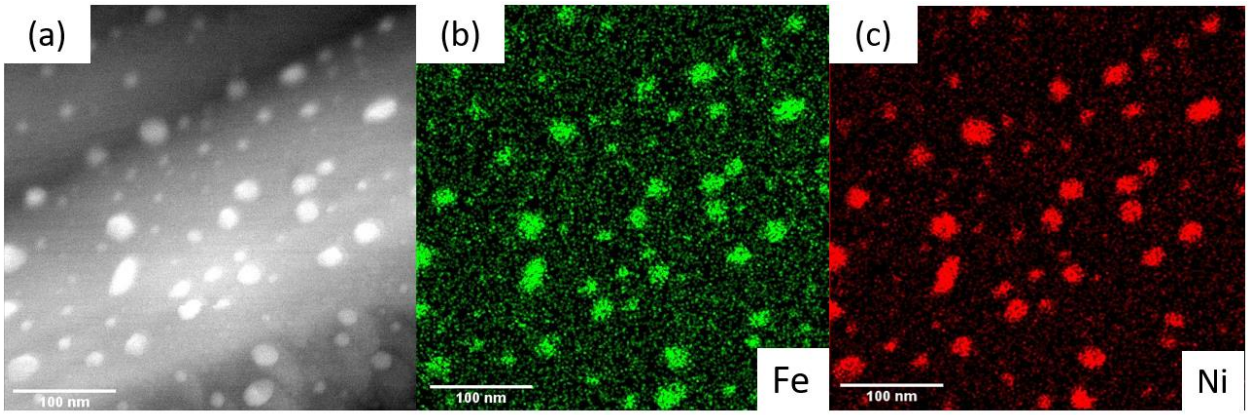

Figure 6: EDX mapping of a TEM micrograph on the TiAl grain showing compositions and distributions of the nano-precipitates on the grain. (a) TEM micrograph of a TiAl grain showing white "dots" distributed throughout, (b) Distribution of the iron element on the grain where "green" indicates the presence of iron, and (c) Distribution of nickel element on the grain where "red" indicates the presence of nickel.

4.4. Quasi-static uniaxial compression

Shown in Figure 7 is a typical stress-time plot of the cermet obtained from the MTS test. The material is loaded uniaxially in the vertical direction. In total, ten experiments are performed to verify repeatability. The nominal strain rate is approximately 10^{-4} s^{-1} in all experiments. This is obtained from calculating the strain by tracking the edge displacements of the specimen among a sequence of images and then dividing by the corresponding time. A brittle-like stress history with constant slope is observed in all experiments (see stress-time in Figure 7 on left). The peak stress in this case, which is often referred as the "quasi-static compressive strength", is measured at 2563

MPa. Over all ten quasi-static experiments, the strength of the $TiAl/Ti_3Al/Al_2O_3$ cermet is measured at 2403 ± 120 MPa.

Next, we examine time-resolved images of the failure process during quasi-static compression on the right of Figure 7. A total of 6 images are shown with times corresponding to those labeled in the stress-history on the left. In the images, no surface cracks are observed during loading (frames 1 to 5), and the material remains intact under the compressive load. At image 5, the failure strain is measured between 1.1% to 1.7%, with an average of 1.4 ± 0.2% among all ten experiments. This is calculated by tracking the edge displacements for the first and last image. The drawback from the edge tracking technique is that it introduces errors based on the image resolution. In this case, the accuracy of the measurement in each test could be deviated up to ~ 0.08% (based on a resolution of 1280 x 1024 and taking half of a pixel width from each side of the edges). Frame six demonstrates a typical failure path of the specimen, taken just after the peak load. At time #6, the material fails catastrophically, and large structural fragments are observed in the corresponding image. An angled major crack passes through the entire specimen, which is believed to be intergranular fracture along the "coral" alumina network. From all quasi-static experiments, the angles of the fractures are 54 ± 3 degrees (measured from the top edge), and these typically form from 4 to 8 larger recoverable fragments.

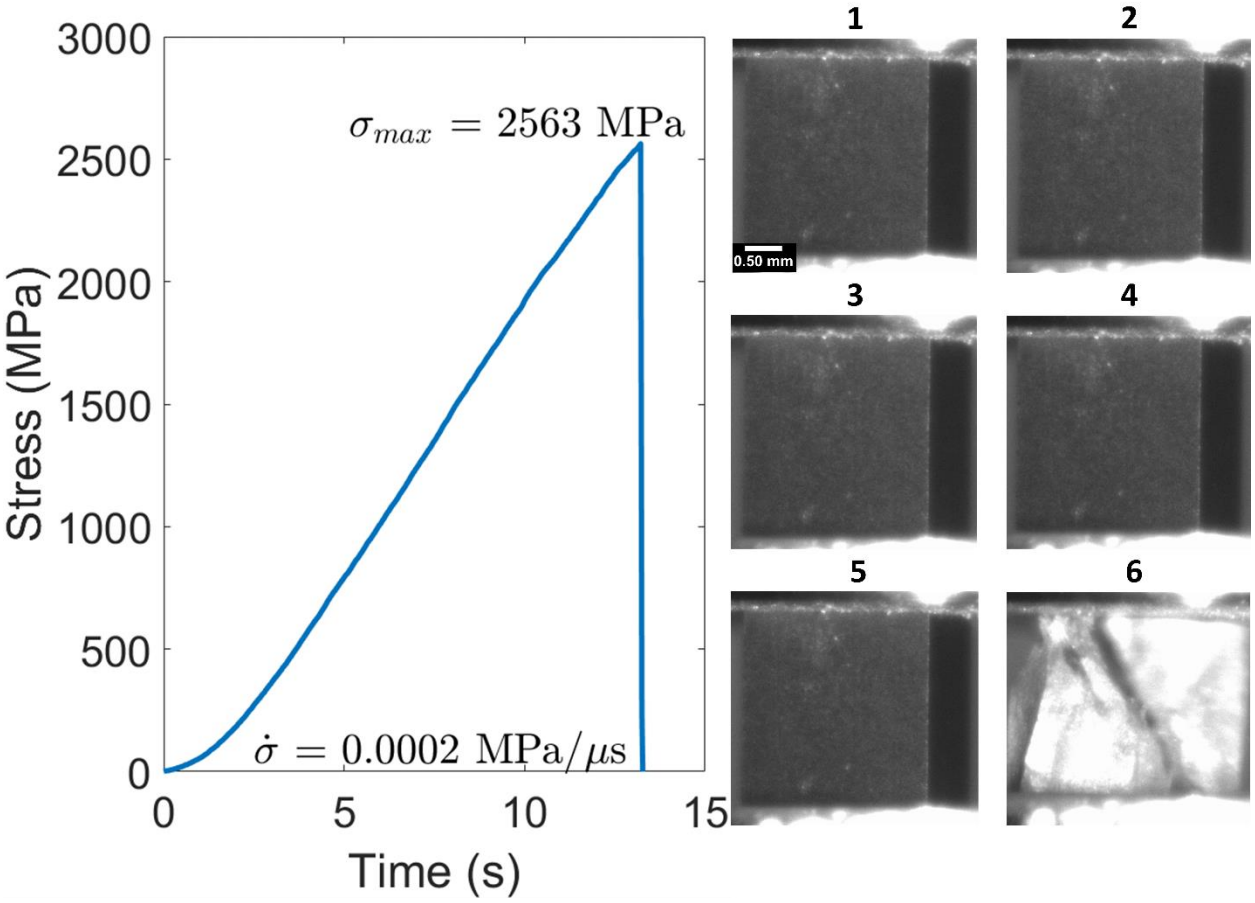

Figure 7: Stress history in quasi-static uniaxial compression with corresponding images at six different times showing the failure process of the material.

4.5. Dynamic uniaxial compression

Shown in Figure 8 is a typical stress history plot of the cermet from the dynamic test. The material is dynamically loaded in the horizontal direction. In Figure 8, the images on the right are re-oriented so that loading is in the vertical directions and the bar is impacting from the bottom towards the top for better visual comparison with the quasi-static case. In total, five experiments are performed to verify the repeatability. For dynamic loading, a different stress history profile is observed than under the quasi-static loading condition. The stress rate, in this case, is 208 MPa/μs, and this is estimated by taking the slope of the linear portion before the stress reaches its first peak. Consequently, the strain rate could be estimated by taking the stress rate and dividing by the intact

elastic modulus of the material. In this case, the strain rate is around 740 s^{-1}. This method of estimation had been used in literature for brittle materials [36]. In all five experiments, the strain rates are in the range of 700 s^{-1} to 1600 s^{-1}. The variability in the strain rate comes from the differences in the projectile speed under the same pressure, as well as the response of the material to the loading. It is observed that the signal peaks appear to ramp up, where the final peak indicates the highest stress reached. The "dynamic compressive strength" is taken as the highest peak stress value, and this is 2903 MPa. Across all experiments, the peak strength was measured as 3370 ± 450 MPa.

Next, we explore time-resolved images depicting dynamic failure in Figure 8. Again, there are six images shown with times corresponding to those labeled in the stress-history on the left. In frame 1, no cracking is observed on the surface. Frame 2 corresponds to the first peak on the curve, where texturing (indicated by cycles in dash line in the current and subsequent frames) is observed on the surface from frame 2 to frame 4. No specific orientation of the texture can be determined. As a consequence of the texturing, relaxation allows the stress to drop from frame 2 to 3. In frame 3, a primary crack (red arrow) is observed at the bottom right corner, this is followed by further texturing with increasing sizes (and hardening in the stress-time curve) from frame 3 to 4. While the stress rises from point 3 to 4, in frame 4, the primary crack propagates axially when the stress raises again to around 2.7 GPa. In frame 5, a secondary crack (blue arrow) branches out from the primary crack, and a second crack (blue arrow) starts to form at the top left corner. In frame 6, more secondary cracks (blue arrow) are formed and branch out, and this results in catastrophic failure. The primary cracks propagate in such a way that they tend to cross the specimen with an angle between 50 and 60 degrees (measured from top edge of the specimen), which coincides with the crack growing direction in the quasi-static case (see Fig. 7 frame 6). The failure strain under

dynamic loading is determined from the frames right before the first crack is observed, and it is measured to be between 3% and 3.3%, with an average of 3.1 ± 0.1% in all five experiments. This is approximately twice as much as the values reported in the quasi-static case. Similar to the quasi-static experiments, the error from the edge tracking method in each measurement could deviate up to ~ 0.25% (based on a resolution of 400 x 250 pixels and taking half of a pixel at each side). Improvements need to be made in the future to accurately measure the strains using, for instance, the digital image correlation (DIC) method in order to increase the accuracy of such measurements. Crack speeds in all five experiments are between 700 m/s and 1200 m/s by measuring the first three primary and secondary cracks observed in each video. The average crack speed is 960 ± 210 m/s. These are estimated by first determining the location of the crack tip in the first frame and then measuring the displacement of the crack tip in subsequent frames. The crack speed of a specific crack is averaged over multiple frames to improve accuracy.

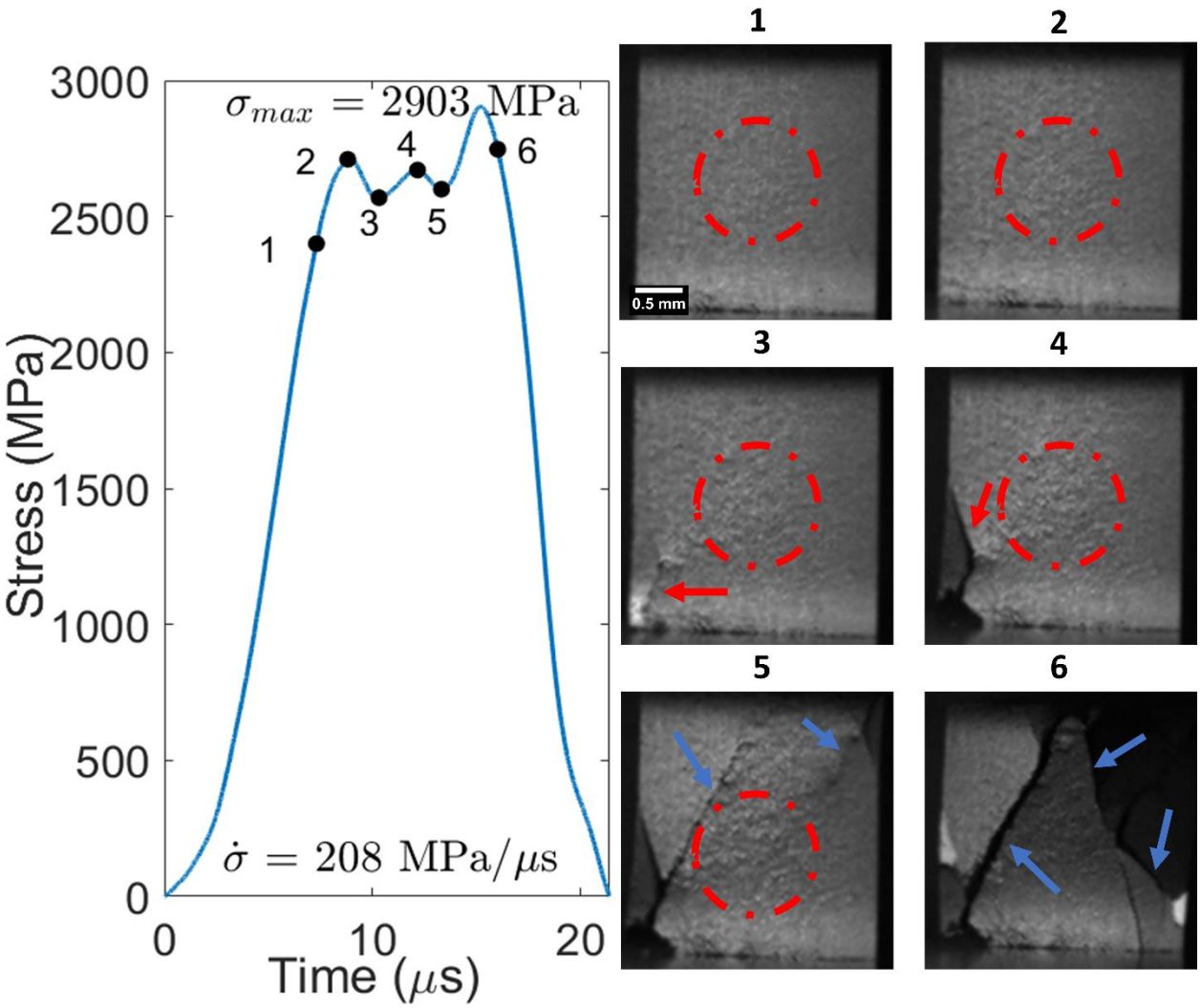

Figure 8: Stress history in dynamic (SHPB) uniaxial compression with corresponding images at six different times. The red arrow shows the formation of the primary crack, the blue arrows shows the formation of the secondary cracks, and the dashed circle indicates the formation of the texturing.

4.6. Summary of the rate-dependent compressive strengths

Shown in Figure 9 is a summary of the compressive strength against strain rate for the TiAl/Ti_3Al/Al_2O_3 cermet. All experiments, including ten quasi-static and five dynamic tests, are plotted against the log scale of the strain rate. For the quasi-static experiments, the rates are approximately 10^{-4} s^{-1}. For the dynamic experiments, the strain rates are 700 s^{-1} to 1600 s^{-1}. It is observed that the dynamic compressive strengths are higher than those in the quasi-static cases.

The quasi-static compressive strength has an average of 2400 ± 120 MPa, and the dynamic compressive strength has an average of 3370 ± 450 MPa. On average, this results in a 1.5 times increase in strength between the strain rate of 10^{-4} s^{-1} to ~ 10^{3} s^{-1}. It is also observed that the strain rate dependency has a more profound effect on the compressive strength in the dynamic regime (> 10^{2} s^{-1}).

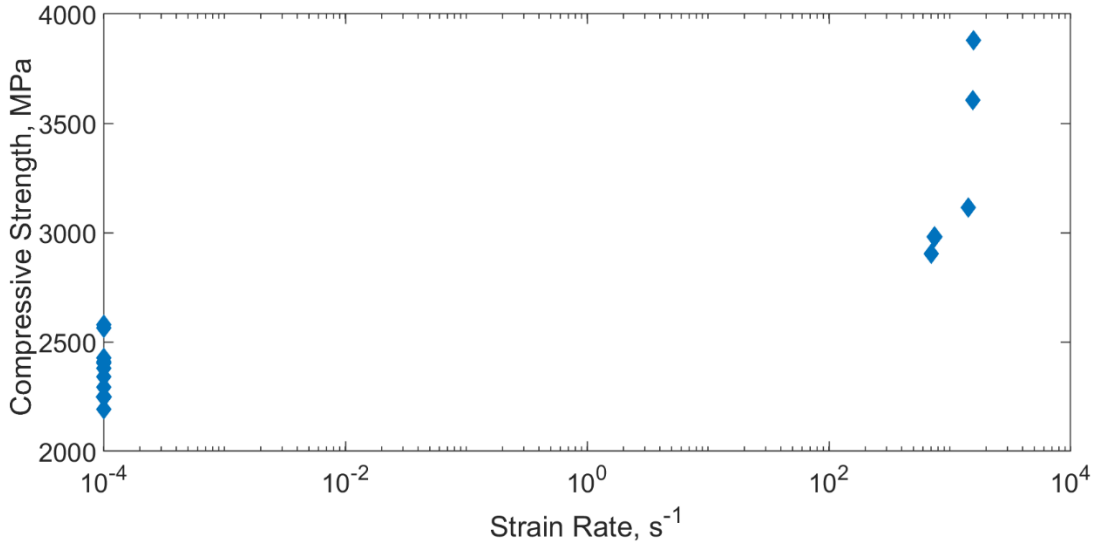

Figure 9: Semi-log plot of the compressive strength of the cermet with respect to the strain rates under uniaxial loading.

5. Discussion

This paper presents results on the characterization and mechanical testing of a SHS manufactured $TiAl/Ti_3Al/Al_2O_3$ cermet. Material composition, phase distribution, microstructure, and nanostructure were characterized using various microscopic diagnoses. The rate dependency on the compressive strength and failure mechanism were explored using quasi-static and dynamic uniaxial compression experiments. In the first part of the discussion section, each part of the characterization works will be bridged with previous studies on similar materials to understand the cermet microstructure further and apply this knowledge to material design. In the second part of

385 the discussion section, the mechanical and failure properties of the cermet will be contrasted with alumina AD995, and implications will be discussed.

5.1. Characterization on the micro/nanostructure and composition of the TiAl/Ti_3Al/Al_2O_3 cermet

Many studies on the TiAl/Ti_3Al/Al_2O_3 cermet have been focused on processing and sintering. For example, Huy et al. [20] investigated the microstructure, hardness and fracture toughness of the Ti_3Al/Al_2O_3 cermet manufactured under an in-situ combustion process. In other studies, Zhu et al.
390 [22] discussed the transitional reaction process in reaction sintering of the TiAl/Al_2O_3 cermet. Shen et al. [17] investigated the electronic structure of the titanium aluminides-alumina cermet from an in-situ SHS process. The summary to date of this material points to the need to develop a detailed report on the micro/nanoscale features. The microstructure of the material needs to be examined in all aspects in order to establish the relationship between microscopic features and mechanical
395 properties. The current paper presents a more detailed characterization work to better summarize the microscopic features of the material.

In the present study, we initially examined the microscale features of the cermet by using SEM, EDS, and XRD. It was found that a heterogeneous microstructure can be achieved by the SHS process, and the alumina phase contributed 65 ± 1% in composition. A "coral" network was
400 defined to describe the connected alumina particle clusters within our TiAl/Ti_3Al/Al_2O_3 cermet. In EDS mapping, it was confirmed that oxygen existed in regions with high concentrations of titanium, and this provided the proof of the existence of α_2-phase that was shown in the XRD results. By consulting the ternary phase diagram of the Al-Ti-O system [37], the current cermet with an oxygen-rich α_2-phase of titanium aluminide falls inside the predicted area in which the
405 three phases (γ-TiAl, α_2-Ti_3Al, and Al_2O_3) co-exist based on the overall atomic composition gathered from EDS (see Table. 2). In other studies, Shen et al. [17] and Zhang et al. [38] have

discovered a two-phase ($\gamma + \alpha_2$) lamellar structure to have appeared in the $TiAl/Ti_3Al/Al_2O_3$ cermet, as a result of the co-existence of individual γ and α_2-phases. They concluded that the ($\gamma+\alpha_2$) structure would have a positive effect on the toughness of the cermet, due to the increased oxygen precipitation at the interface. Forouzanmehr et al. [40] fabricated the TiAl/α-Al2O3 by mechanical alloying, where no additional α_2-phase and its corresponding lamellar structure was identified in the material. Numerous SEM studies have also been conducted on similar cermets fabricated by different methods. Fine microstructures of the $TiAl/Ti_3Al/Al_2O_3$ cermet have been produced by Shen et al. [17] using SHS, Zhu et al. [22] using Reaction Synthesis (RS), and Travitzky et al. [39] using Pressure-assisted Thermal Explosion. However, the microstructure looked much coarser when fabricated using mechanical alloying [40]. Huy et al. [20] discovered a similar alumina "coral" network as the current cermet under 1173 K with Combustion Sintering (CS). It is believed that the SHS process can be one of the best manufacturing techniques for generating such cermets in significantly short sintering times, where the existence of the α_2-phase is guaranteed. This information is valuable in material design and manufacturing, where the microstructure and composition of the material can be tied back to the fabrication methods. To further elaborate, the existence of the α_2-phase, homogeneity, fineness of the microstructure, and state of the alumina phase could all have positive effects on the material performance.

Next, we investigated the nanoscale microstructural features of the cermet. The individual alumina particle sizes were found to be in the sub-micron range with an average of 1.0 ± 0.3 μm. Grain boundaries were found to be free of additives with no microcracks or plastic deformation, while the "coral" network of alumina particles was further examined using EDS. Additionally, TEM analysis on individual grains showed iron-nickel nano-precipitates distributed uniformly throughout the entire material. The nano-precipitates were most likely in the form of metallic and

oxide of iron and nickel [32 – 35]. In the literature, Kamali et al. [21] have shown the capability of controlling the grain size of the $TiAl/Al_2O_3$ cermet by adding $KClO_4$ to the mixture of the starting powders (TiO_2/Al). In other cermets, the effects of nano-precipitates on the mechanical properties of cermets have been studied. For example, Zhang et al. [41] discovered that the addition of nano-Si3N4 particles had shown improvements on the hardness and transverse rupture strength of the Ti (C, N)-based cermet by 1.3% and 25.2%, respectively. Other studies have shown abilities in improving Rockwell hardness, fracture toughness, and flexural strength by tailoring microstructure with nano-powders in TiC-based and TiAl-based cermets [19] [42] [43]. The effect of iron/nickel nano-precipitates on the behavior of the current cermet is yet to be determined. Overall, these findings encourage material design, which could give various enhancements based on industrial needs, including controlling the grain size by changing the phase compositions or adding nano-precipitates, where the mechanical properties of the final product could be tailored as well.

5.2. Rate-dependent failure mechanisms

In this section, the rate-dependent failure mechanisms of the cermet are discussed in terms of the stress-time responses and cracking behavior. In the present study, clear differences can be seen from the stress-history curve under the different loading rates. The quasi-static stress response exhibited similar behavior to that of the elastically deformed ceramics, where a linear increase in the stress-time profile was observed. The peak stress was reached without observing any surface deformation or cracking. In contrast for dynamic loading, the material exhibited plastic deformation, where several rises and drops of the stress were observed in the stress-time history curve. This is believed to be the result of the alternating thermal softening and strain hardening phenomena in the $TiAl/Ti_3Al$ matrix (confirmed through imaging which is discussed next). This

has been observed previously by Wu et al. [44] during adiabatic shear banding in 7003-T4 aluminum alloy under high strain rate impact. It is believed that the heat accumulates locally in the specimen during high rate loading, which results in thermal softening of the titanium aluminide phase and contributes to local crack initiation. However, this can be overcome by strain or strain rate hardening, where texturing was observed in our $TiAl/Ti_3Al/Al_2O_3$ cermet before crack initiation and catastrophic failure. In other ceramic studies, the stress-history behavior of the ceramic under dynamic loading was significantly different, where a linear elastic triangular pulse was observed [45 – 47]. This gives further proof for the hypothesis that additional deformation mechanisms other than brittle fracture occur in the current cermet during dynamic loading. However, texturing coupled with thermal softening can be a potential disadvantage in ballistic performance since the material will be softened for a certain amount of time (in terms of microseconds) during loading, and this will significantly decrease the duration of the dwelling phase. As a result, more energy will be transferred to the deeper layer of armor without enough destruction of the projectile [48] [49]. Future improvement on the material design perspective should be directed towards minimizing this effect.

Next, high-speed imaging revealed strain-rate dependent failure mechanisms. Quasi-statically, cracking always followed a path with the fracture angle of 54 ± 3 degrees (measured from the top edge) (see Fig. 7 image 6) across the whole specimen upon failure, and no crack branching was observed. It is believed that the cermet fails majorly through intergranular fracture at low strain rates. Crack propagation will likely follow along with the "coral" alumina network and alumina grain boundaries in the material, and the onset of failure could be from interfacial flaws or micro-pores. In contrast, texturing was observed on the material surface in dynamic loading before and during cracking (see Fig. 8 image 1-4). In addition, several primary and secondary crack branches

were observed (see Fig. 8 image 3-6). In all experiments, the primary cracks propagate with an angle between 50 and 60 degrees towards the center of the specimen, while random branching occurred during further loading. It is believed that the material fails through a combination of intergranular and transgranular cracking along and through the alumina phase. This is because more kinetic energy is introduced into the material during impact, which allows cracks to propagate through the much harder alumina grains with a much smaller time scale. The crack speeds of the cermet were measured at 700 m/s to 1200 m/s under dynamic loading with an average of 960 ± 210 m/s. Note that only crack speeds for the dynamic loading case are considered here because the quasi-static cracking could not be measured with the current setup. Similar mechanisms have been identified in the TiC/Steel cermet with the aid of TEM by Kaplan et al. [11]. It was found that transgranular fracture was the dominant failure mechanism under dynamic loading, and micro-crack toughening was found to be another mechanism, which extensively contributes to dynamic failure. When compared to advanced ceramics, Acharya et al. [50] studied the failure mechanism of AD995 under high strain rate loading and reported that plasticity, such as dislocation array and transgranular microcracking could occur, resulting in failure. These mechanisms may also be activated in the nano-grained alumina in our cermet, as well as other plastic deformation mechanisms in the titanium aluminide phase (e.g., twining and dislocation) [62 - 65]. In addition, the fragmentation behavior of the cermet is vastly different from what is observed in some typical advanced ceramics. For the cermet, less cracking and larger structural fragments were found after failure. When compared with ceramics such as shown in Hu et al. [28] for aluminum nitride and Hogan et al. [51] for silicon carbide, much denser cracks were observed at the onset of failure, and the material seemed to powder and explode upon catastrophic failure.

This particular feature of the cermet can, perhaps, be beneficial in multi-hit capacity for body armor if proper confinement is established.

5.3. Comparison of the rate-dependent mechanical properties with alumina AD995

In this section, the compressive strength of the cermet is discussed in the context of comparison with alumina AD995 (refer as AD995 later in the text) manufactured by Coorstek Inc., which is a typical advanced ceramic being used as insert in body armors that has a similar density as the TiAl/Ti_3Al/Al_2O_3 cermet (~ 3.9 g/cm^3). To do this, we show the strength-strain rate plot of AD995 and the TiAl/Ti_3Al/Al_2O_3 cermet in Figure 10. The AD995 data have been gathered from both experiments conducted in the lab by using the same experimental setup and as well as data results collected from the literature [45] [50] [52]. In the cermet experiments, the quasi-static compressive strength of the cermet has an average of 2400 ± 120 MPa, while the dynamic compressive strength has an average of 3370 ± 450 MPa. This gives approximately 1.5 times increase in strength with a seven order increase in strain rate. For the rate-dependency on compressive strength of other cermets, Mandel et al. [12] and Marchi et al. [61] found an approximately 1.5 times increase in strength in the WC-Co system (from 4370 MPa to 6660 MPa with 10^{-4} s^{-1} to 10^3 s^{-1} strain rate) and 55 vol% Al_2O_3/Al cermet (from ~ 400 MPa to ~ 600 MPa with 10^{-4} s^{-1} to 10^3 s^{-1} strain rate), respectively. Guden and Hall [13] and Zhu et al. [60] also found an approximately 1.3 times increase in the 35 vol% Al_2O_3/Al (from ~ 260 MPa to ~ 340 MPa with 10^{-3} s^{-1} to 10^3 s^{-1} strain rate) and TiB_2/Al (From ~ 900 MPa to ~ 1200 MPa with 10^{-4} s^{-1} to 10^3 s^{-1} strain rate) cermets, respectively. Similarly, the quasi-static compressive strength of AD995 has an average of 2444 ± 247 MPa, while the dynamic compressive strength has an average of 3590 ± 493 MPa. This gives approximately 1.5 times increase as well. The order of increase in the compressive strength of these materials is comparable. In conclusion, clear rate-dependency on compressive strength can

be observed in both TiAl/Ti_3Al/Al_2O_3 cermet and AD995, and the current cermet has comparable strength with AD995 under both loading conditions. This is important to note because compressive strength has been identified to be important by some in ballistic protection applications [53].

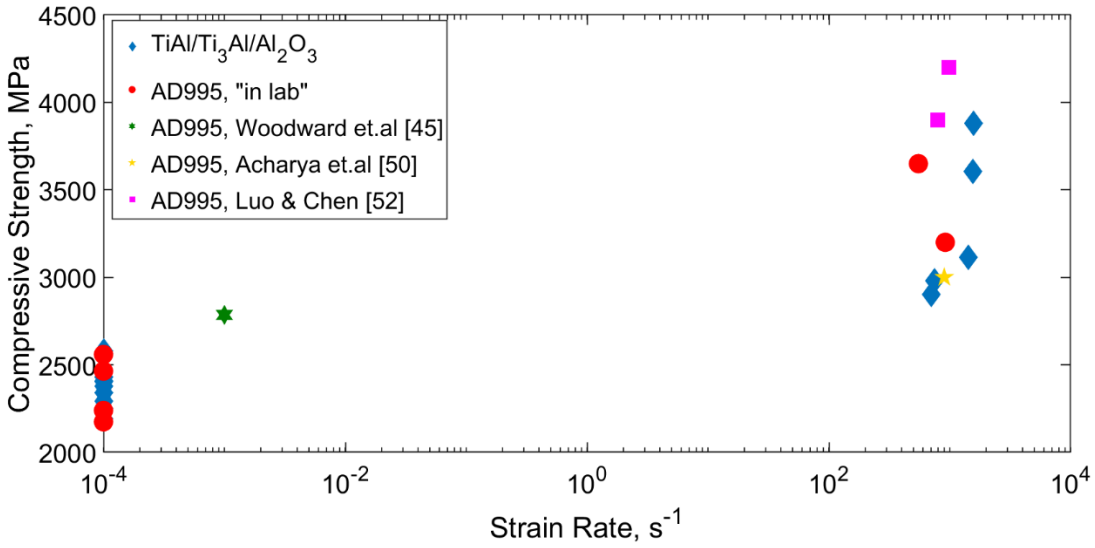

Figure 10: Summary of the compressive strength of the cermet with respect to strain rate under uniaxial compression with comparison to alumina AD995 manufactured by Coorstek. The alumina data was gathered from both experiments conducted in the author's lab and data reported in literature.

Lastly, the failure strain was measured under both loading rates. The average failure strains of the cermet are 1.4 ± 0.2% and 3.1 ± 0.1% under quasi-static and dynamic uniaxial loading, respectively. For other cermets, such as WC/Co, TiC/Ni, Al_2O_3/Cr, and B_4C/Al, the failure strains were between 0.3% and 2.0% quasi-statically depending on the composition [54 – 56]. Failure strain of the TiAl/Ti_3Al/Al_2O_3 cermet falls at the higher end of this range, which points to some positive aspects of this materials. Lankford [46], Luo and Chen [52], and Krell and Strassburger [53] have conducted SHPB experiments on AD995 to assess the dynamic behavior. In those studies, the dynamic failure strain was between 1.0% to 1.5%, whereas the quasi-static failure strain was measured between 0.5% to 0.8% from the tests presented in Figure 10. The failure strain of the

$TiAl/Ti_3Al/Al_2O_3$ cermet is more than twice higher than AD995 under both loading conditions. One drawback of advanced ceramics like AD995 is that the brittleness of the material limits its ballistic performance, where catastrophic failure after the dwelling phase does not provide significant energy dissipation, and a thick metallic backing plate is usually needed [4]. With cermets being developed, ductility is introduced into the material to potentially overcome this limitation [4] [5]. For our $TiAl/Ti_3Al/Al_2O_3$ cermet, the fracture toughness of the material has been significantly improved over alumina based on the data provided by the manufacturer (see Table. 1), while texturing has been observed under dynamic loading (see Fig. 8). It needs to be noted that the occurrence of plasticity and increase in toughness of the cermet should be examined in a more systematic way with fractography (SEM/TEM) and the stress-strain curves. The conclusion presented above is based on published data and observations on surface deformation. In summary, since damage tolerance capacity and hardness are both critical factors in determining the efficiency of energy dissipation and mass defecation during perforation, there is a need to identify the best trade-off between hardness and fracture toughness to further improve the ballistic efficiency of body armors.

6. Concluding remarks

In this study, the behavior of the $TiAl/Ti_3Al/Al_2O_3$ cermet was investigated using microscopic characterization and mechanical testing. Detailed characterization, including scanning electron microscopy and transmission electron microscopy, revealed the microstructural and nanostructural features, where a “coral” network of alumina particles was identified. Energy-dispersive X-ray spectroscopy and x-ray diffraction identified the phase composition and elemental concentration of the cermet, where it was found to contain γ-TiAl, Al_2O_3, and an additional α_2-Ti_3Al phase was found as a by-product in the SHS process. Iron and nickel-based nano-precipitates were also found

throughout the material. The rate-dependent stress-strain response, compressive strength, and failure mechanisms were investigated by quasi-static and dynamic uniaxial compression coupling with high-speed imaging, where alumina AD995 was used as a reference for comparison. Comparable compressive strengths, higher failure strains, and larger structural fragments were identified for the $TiAl/Ti_3Al/Al_2O_3$ cermet, when compared to AD995. In addition, texturing was clearly observed under dynamic loading, and a hypothesis was proposed on the occurrence of plastic deformation taking place in the cermet during failure. The data generated in this study provides guidelines for future material improvement, manufacturing, and simulation.

Data Availability

- The raw/processed data required to reproduce these findings cannot be shared at this time due to technical or time limitations.
- The raw/processed data required to reproduce these findings cannot be shared at this time as the data also forms part of an ongoing study.

Reference

[1] Tsuda, Keiichi. "History of development of cemented carbides and cermet." *SEI Technical Review* 82 (2016): 16-20.

[2] Mari, Daniele. (2001). Cermets and Hardmetals. *Encyclopedia of Materials: Science and Technology.* 1118-1123. 10.1016/B0-08-043152-6/00209-6.

[3] J. Chevalier, L. Gremillard, Ceramics for medical applications: A picture for the next 20 years, *Journal of the European Ceramic Society* 29 (7) (2009) 1245 – 1255.

[4] Wilkins, M. L., C. F. Cline, and C. A. Honodel. *FOURTH PROGRESS REPORT OF LIGHT ARMOR PROGRAM*. No. UCRL-50694. California Univ., Livermore. Lawrence Radiation Lab., 1969.

[5] Landingham, R. L., and A. W. Casey. *Final report of the light armor materials program*. No. UCRL--51269. California Univ., 1972.

[6] Strassburger, E., et al. "Behaviour of Al2O3-Al ceramic metal composites under projectile impact." *Le Journal de Physique IV* 10.PR9 (2000): Pr9-605.

[7] Ischenko, A. N., et al. "Investigation of impact resistance of protective barriers made from cermets." *Russian Physics Journal* 58.9 (2016): 1347-1352.

[8] Loiseau, J., et al. "Ballistic Response of Chromium/Chromium-Sulfide Cermets." *Journal of Dynamic Behavior of Materials*1.3 (2015): 347-358.

[9] Madheswaran, K., S. Sugumar, and B. Elamvazhudi. "Mechanical characterization of Aluminium–Boron carbide composites with influence of Calcium carbide particles." *International Journal of Emerging Technology and Advanced Engineering* 5.7 (2015): 492-496.

[10] Rittel, D., N. Frage, and M. P. Dariel. "Dynamic mechanical and fracture properties of an infiltrated TiC-1080 steel cermet." *International journal of solids and structures* 42.2 (2005): 697-715.

[11] Kaplan, W. D., et al. "Static and dynamic mechanical damage mechanisms in TiC-1080 steel cermets." *Scripta materialia* 51.1 (2004): 37-41.

[12] Mandel, Kristin, Markus Radajewski, and Lutz Krüger. "Strain-rate dependence of the compressive strength of WC–Co hard metals." *Materials Science and Engineering: A* 612 (2014): 115-122.

[13] Guden, M., and Ian W. Hall. "Quasi-static and dynamic compression behaviour of an FP^{TM} alumina-reinforced aluminum metal matrix composite." *Journal of materials science* 33.13 (1998): 3285-3291.

[14] Ramesh, K. T., and G. Ravichandran. "Dynamic behavior of a boron carbide aluminum cermet: experiments and observations." *Mechanics of Materials* 10.1-2 (1990): 19-29.

[15] Blumenthal, W. R., G. T. Gray, and T. N. Claytor. "Response of aluminium-infiltrated boron carbide cermets to shock wave loading." *Journal of materials science* 29.17 (1994): 4567-4576.

[16] Lu, Y. X., et al. "Microstructure and mechanical behaviour of a SiC particles reinforced Al–5Cu composite under dynamic loading." *Journal of materials processing technology* 94.2-3 (1999): 175-178.

[17] Shen, Y. F., et al. "Properties and electronic structures of titanium aluminides–alumina composites from in-situ SHS process." *Materials Science and Engineering: A* 528.4-5 (2011): 2100-2105.

[18] Xiang, Liuyi, et al. "Mechanical properties and microstructure of Al2O3/TiAl in situ composites doped with Cr2O3." *Materials Science and Engineering: A* 528.9 (2011): 3337-3341.

[19] Zhang, Kun, et al. "The Microstructures and Mechanical Properties of V 2 O 5-Doped Al 2 O 3/TiAl In-Situ Composites by Reactive Hot Pressing Process." *Journal of materials engineering and performance* 22.12 (2013): 3933-3939.

[20] Huy, Tran Duc, et al. "Microstructure and Mechanical Properties of TiAl3/Al2O3 in situ Composite by Combustion Process." *Materials Transactions* 55.7 (2014): 1091-1093.

[21] Kamali, Ali Reza, et al. "Production of TiAl (Ti3Al)/Al2O3 Nanocomposite." *Journal of Nano Research*. Vol. 3. Trans Tech Publications, 2008.

[22] Zhu, Jian Feng, Ji Qiang Gao, and Fen Wang. "Reaction Synthesis of TiAl-Al2O3 Composite." *Key Engineering Materials*. Vol. 336. Trans Tech Publications, 2007.

[23] Gaus, Shaun P., et al. "Alumina–Aluminide Alloys (3A) Technology: II, Modeling of TixAly–Al2O3 Composites Formation." *Journal of the American ceramic society* 83.7 (2000): 1606-1612.

[24] "Advanced-Alumina-Brochure." Coorstek.Inc, 2016. https://www.coorstek.com/media/1715/advanced-alumina-brochure.pdf

[25] "Ultra Nanoindentation Tester (UNHT³)." Anton Paar, www.anton-paar.com/ca-en/products/details/ultra-nanoindentation-tester-unht3/.

[26] ASTM C1425-15. Standard test method for monotonic compressive strength of advanced ceramics at ambient temperature, West Conshohocken (PA).

[27] Hogan, James David, et al. "The effects of defects on the uniaxial compressive strength and failure of an advanced ceramic." *Acta Materialia* 102 (2016): 263-272.

[28] Hu, Guangli, et al. "The compressive failure of aluminum nitride considered as a model advanced ceramic." *Journal of the Mechanics and Physics of Solids* 59.5 (2011): 1076-1093.

[29] Chen, Weinong, and G. Ravichandran. "Dynamic compressive failure of a glass ceramic under lateral confinement." *Journal of the Mechanics and Physics of Solids* 45.8 (1997): 1303-1328.

[30] Chen, Weinong W., and Bo Song. *Split Hopkinson (Kolsky) bar: design, testing and applications*. Springer Science & Business Media, 2010.

[31] Xia, Kaiwen, and Wei Yao. "Dynamic rock tests using split Hopkinson (Kolsky) bar system–A review." *Journal of Rock Mechanics and Geotechnical Engineering* 7.1 (2015): 27-59.

[32] Raghavan, V. "Al-Ni-Ti (aluminum-nickel-titanium)." *Journal of Phase Equilibria and Diffusion* 26.3 (2005): 268-272.

[33] Marker, Martin CJ, et al. "Characterization of the Fe-rich corner of Al–Fe–Si–Ti." *Intermetallics* 39 (2013): 38-49.

[34] Fadhil, Alaa Hassan, Mohsin A. Aswad, and Ahmed O. Al-Roubaiy. "THE STUDY OF THE THERMAL PROPERTIES OF SPINEL NICKEL ALUMINATE." *Iraqi journal of mechanical and material engineering* 16.1 (2016): 45-59.

[35] Dreval, Liya, Tilo Zienert, and Olga Fabrichnaya. "Calculated phase diagrams and thermodynamic properties of the Al2O3–Fe2O3–FeO system." *Journal of Alloys and Compounds* 657 (2016): 192-214.

[36] Chen, W., G. Ravichandran, and K. T. Ramesh. "A single pulse loading technique using the split Hopkinson pressure bar." *SM Report* (1995): 95-12.

[37] Das, Siddhartha. "The Al-O-Ti (aluminum-oxygen-titanium) system." *Journal of Phase Equilibria* 23.6 (2002): 525-536.

[38] Zhang, Kun, et al. "The Microstructures and Mechanical Properties of V 2 O 5-Doped Al 2 O 3/TiAl In-Situ Composites by Reactive Hot Pressing Process." *Journal of materials engineering and performance* 22.12 (2013): 3933-3939.

[39] Travitzky, N., I. Gotman, and N. Claussen. "Alumina–Ti aluminide interpenetrating composites: microstructure and mechanical properties." *Materials Letters* 57.22-23 (2003): 3422-3426.

[40] Forouzanmehr, N., F. Karimzadeh, and M. H. Enayati. "Synthesis and characterization of TiAl/α-Al2O3 nanocomposite by mechanical alloying." *Journal of Alloys and Compounds* 478.1-2 (2009): 257-259.

[41] Zhang, Houan, Ji-yong Yi, and Si-yong Gu. "Mechanical properties and microstructure of Ti (C, N) based cermets reinforced by nano-Si3N4 particles." *International Journal of Refractory Metals and Hard Materials* 29.2 (2011): 158-162.

[42] Xiang, Liuyi, et al. "Mechanical properties and microstructure of Al2O3/TiAl in situ composites doped with Cr2O3." *Materials Science and Engineering: A* 528.9 (2011): 3337-3341.

[43] Zhang, Houan, Siyong Gu, and Jiyong Yi. "Fabrication and properties of Ti (C, N) based cermets reinforced by nano-CBN particles." *Ceramics International* 38.6 (2012): 4587-4591.

[44] Wu, Xiaodong, et al. "Development of adiabatic shearing bands in 7003-T4 aluminum alloy under high strain rate impacting." *Materials Science and Engineering: A* (2018).

[45] Woodward, R. L., et al. "A study of fragmentation in the ballistic impact of ceramics." International Journal of Impact Engineering 15.5 (1994): 605-618.

[46] Lankford Jr, James. "The role of dynamic material properties in the performance of ceramic armor." *International Journal of Applied Ceramic Technology* 1.3 (2004): 205-210.

[47] Chen, Weinong, and Huiyang Luo. "Dynamic compressive testing of intact and damaged ceramics." *27th Annual Cocoa Beach Conference on Advanced Ceramics and Composites-A*. Vol. 268. John Wiley & Sons, 2009.

[48] Huang, Feng-Lei, and Lian-Sheng Zhang. "Investigation on ballistic performance of armor ceramics against long-rod penetration." *Metallurgical and Materials Transactions A* 38.12 (2007): 2891-2895.

[49] Lundberg, Patrik, René Renström, and Bengt Lundberg. "Impact of metallic projectiles on ceramic targets: transition between interface defeat and penetration." *International Journal of Impact Engineering* 24.3 (2000): 259-275.

[50] Acharya, Saikat, et al. "Deformation and failure of alumina under high strain rate compressive loading." *Ceramics International* 41.5 (2015): 6793-6801.

[51] Hogan, James David, et al. "On compressive brittle fragmentation." *Journal of the American Ceramic Society* 99.6 (2016): 2159-2169.

[52] Luo, Huiyang, and Weinong Chen. "Dynamic compressive response of intact and damaged AD995 alumina." *International Journal of Applied Ceramic Technology* 1.3 (2004): 254-260.

[53] Krell, Andreas, and Elmar Strassburger. "Order of influences on the ballistic resistance of armor ceramics and single crystals." *Materials Science and Engineering: A* 597 (2014): 422-430.

[54] Kerper, Matthew J., et al. "Evaluation of tensile, compressive, torsional, transverse, and impact tests and correlation of results for brittle cermets." *Journal of Research of the National Bureau of Standards* 61.3 (1958): 149.

[55] Johnson Jr, Aldie E. "Mechanical properties at room temperature of four cermets of tungsten carbide with cobalt binder." (1954).

[56] Blumenthal, William R. "High strain rate compression testing of ceramics and ceramic composites." *Advances in Ceramic Armor: A Collection of Papers Presented at the 29th International Conference on Advanced Ceramics and Composites, Jan 23-28, 2005, Cocoa Beach, FL*. Vol. 296. John Wiley & Sons, 2009.

[57] Frew, D. J., M. J. Forrestal, and W. Chen. "Pulse shaping techniques for testing elastic-plastic materials with a split Hopkinson pressure bar." *Experimental mechanics* 45.2 (2005): 186.

[58] Naghdabadi, R., M. J. Ashrafi, and J. Arghavani. "Experimental and numerical investigation of pulse-shaped split Hopkinson pressure bar test." *Materials Science and Engineering: A* 539 (2012): 285-293.

[59] Vecchio, Kenneth S., and Fengchun Jiang. "Improved pulse shaping to achieve constant strain rate and stress equilibrium in split-Hopkinson pressure bar testing." *Metallurgical and materials transactions A* 38.11 (2007): 2655-2665.

[60] Zhu, Dezhi, et al. "Dynamic deformation behavior of a high reinforcement content TiB2/Al composite at high strain rates." *Materials Science and Engineering: A* 487.1-2 (2008): 536-540.

[61] San Marchi, C., et al. "Quasi-static and dynamic compression of aluminum-oxide particle reinforced pure aluminum." *Materials Science and Engineering: A* 337.1-2 (2002): 202-211.

[62] Appel, F. "An electron microscope study of mechanical twinning and fracture in TiAl alloys." *Philosophical Magazine*85.2-3 (2005): 205-231.

[63] Marketz, W. T., F. D. Fischer, and H. Clemens. "Deformation mechanisms in TiAl intermetallics—experiments and modeling." *International Journal of Plasticity* 19.3 (2003): 281-321.

[64] Ji, Zong-Wei, et al. "Mapping deformation mechanisms in lamellar titanium aluminide." *Acta Materialia* 144 (2018): 835-843.

[65] Guo, Wenqi, et al. "Nanoscale Twinned Ti-44Al-4Nb-1.5 Mo-0.007 Y Alloy Promoted by High Temperature Compression with High Strain Rate." *Metals* 8.8 (2018): 619.